We acknowledge that this submission of:

'Minkowski Functionals as Analytical Predictors of Permeability in Porous Microstructures'

Is a non-peer-reviewed preprint submitted to EarthArXiv

18-09-2025

Sijmen Zwarts	s.zwarts@tudelft.nl
Winston Lindqwister	w.lindqwister@tudelft.nl
Martin Lesueur	m.lesueur@tudelft.nl

Minkowski Functionals as Analytical Predictors of Permeability in Porous Microstructures

Sijmen Zwarts[a,*], Winston Lindqwister[a], Martin Lesueur[a]

[a] *Civil Engineering and Geosciences, Delft University of Technology, Delft, Netherlands*

Abstract

Understanding the relationship between microstructure and macroscopic properties in porous media remains crucial for numerous applications in geoscience and engineering. For example, accurate predictability of permeability is essential for optimizing fluid flow processes in applications such as hydrocarbon recovery, groundwater management, and carbon or energy storage. The Kozeny-Carman equation has long served as a fundamental tool for predicting permeability based on porosity and specific surface area, with an empirical adjusted constant for different types of materials. Modifications to the equation have been introduced to improve the predictability on selected materials, but they become more specific and introduce new parameters. In this study, we explore an alternative analytical formulation that links permeability directly to Minkowski functionals (MFs), which are known to be more general systematic descriptors of porous media microstructure. Utilizing a database of simulated granular and cemented microstructures, we evaluate permeability predictions based on this MF-based formulation. We show a strong correlation between the functionals and the hydraulic properties, based on very simple assumptions. Despite the motion invariant limitation of the MFs that we confirm in our anisotropic case study, this contribution highlights the potential of MFs as a generalisation of rock typing for permeability prediction.

Keywords: Rock microstructures, Porous Media, Permeability, Fluid flow, Minkowski Functionals

1. Introduction

The relationship between a material's microscopic structure and its macroscopic behaviour represents a fundamental topic of interest in materials science. This relationship is particularly significant in porous media, like rocks, granular and engineered materials, that contain a complex network of voids within a solid matrix. With the rise of new metamaterials, the role and effect of different phases in the microstructure become increasingly critical to investigate. Porous materials play essential roles in groundwater management, carbon sequestration, energy storage, and industrial filtration, where

*Corresponding author
Email address: s.zwarts@tudeltf.nl (Sijmen Zwarts)

their performance depends heavily on structural characteristics. For instance, grain size strongly influences mechanical properties (Hu et al., 2011), while the relationship between porosity and permeability has been extensively studied for optimizing fluid flow applications (Koponen et al., 1997; Hommel et al., 2018).

Permeability stands out as one of the most relevant properties of porous media, particularly given its importance in geosciences. Traditional analytical approaches to understand and predict permeability often simplify the complex pore network into a single channel with a complicated geometry, building upon Poiseuille's law (Sutera and Skalak, 1993). A similar concept is applied to fluid flow in fractures, where permeability is shown to scale with the cube of the aperture (Witherspoon et al., 1980). This simplification of representation, combined with the concept of hydraulic radius to account for complex void network geometries, the actual tortuous path of the flow through the porous material and integrated with Darcy's law (Darcy, 1856), led to the development of the Kozeny-Carman equation (Carman, 1939). This equation has become a cornerstone in the scientific community for predicting permeability based on two fundamental parameters of the microstructure: the specific surface area and porosity of the material. The hydraulic tortuosity and the shape factor are often combined in an empirical determined variable, the Kozeny-Carman parameter, matched to specific materials. The specific surface area can also be related to certain grain shapes, leading to expressions with the average grain diameter included, which can be commonly found within the literature (McCabe et al., 1967; Torskaya et al., 2014; Safari et al., 2021). The Kozeny-Carman equation has been widely successful in predicting permeability for homogeneous granular media such as sandpacks and unconsolidated sediments, offering reliable estimates over a range of porosities and grain sizes (Heijs and Lowe, 1995; Chapuis and Aubertin, 2003; Bear, 1972).

While the Kozeny-Carman equation remains the industry standard, it has undergone numerous modifications to better capture diverse microstructural characteristics. One significant line of development focuses on flow path complexity, with researchers like Nooruddin and Hossain (2011) and Yazdchi et al. (2011) incorporating tortuosity approximations into the equation. Surface properties have been studied with Zhong et al. (2023) proposing correction factors for active surface properties and Nomura et al. (2018) incorporating specific surface area measurements. Another important direction explores particle characteristics, as Panda and Lake (1994) and Ye et al. (2022) account for soil particle size distribution, Koponen et al. (1997); Kazemi et al. (1976); Peaceman (1976); de Swaan (1990); Hu et al. (2020) introduce specific shapes of particles, and Liu and Jeng (2019) integrates grain particle size. Recent work has expanded to address structural heterogeneity, with Li et al. (2018, 2023) examining anisotropy and Lei et al. (2023) investigating heterogeneous microstructures. While these modifications have advanced our understanding, they often introduce material-specific parameters, highlighting the need for a more generalised approach to microstructural description. In this paper, we focus on a more general way of predicting permeability. The Kozeny–Carman equation rests on assumptions of a granular microstructure. However, porous media with a solid skeleton, such as metamaterials or rock microstructures, deviate from this picture because of their structural rigidity.

Minkowski functionals provide this systematic method to describe the topological and geometrical features of microstructures in general, including porosity M_0, surface area M_1, mean curvature M_2, and the Euler characteristic M_3. The functionals originate

from integral geometry, offering a rigorous framework to characterise different aspects of Euclidean bodies. Recent research has highlighted the growing application of Minkowski functionals as robust descriptors of microstructures (Santaló and Kac, 2004; Schneider, 2014; Armstrong et al., 2018). Minkowski functionals provide exact quantitative descriptions of morphology, enabling the analysis of specific surface area, structural roughness, and pore connectivity or percolation. A significant advantage of this approach is that these descriptors can be directly measured from image analysis tools without relying on assumptions about the porous medium type.

In fact, Sadeghnejad et al. (2023) demonstrated that the representative elementary volume (REV) convergence of porosity, curvature, and permeability are closely aligned, highlighting strong correlations between microstructural descriptors and physical properties. These findings suggest that MFs may contain sufficient information to characterise permeability. A key question, however, is whether MFs alone can serve as the sole descriptors required for permeability prediction, without relying on additional microstructural measures. While recent advances in data-driven and machine-learning approaches have shown promise in predicting physical properties (Slotte et al., 2020; Jones and Clarke, 2021; Lindqwister et al., 2025), such methods often lack extrapolation power and provide limited physical insight.

Indeed, the different MFs can vary substantially depending on the different structures. Mostaghimi et al. (2012) provides an overview of porosity and specific surface area for various geological samples, including sandpacks, sandstones, and carbonates. Their data reveal that sandpacks exhibit porosities between 33% and 38%, while sandstones and carbonates show lower porosities, often below 14%. Schepp et al. (2020) presents vulcanic rock examples, with porosities over 90%. Specific surface areas in these samples range from 14 mm^2 to 28 mm^2. Similarly, Zubov et al. (2024) highlights the porosities of low-porosity sandstones (12%-22%) and carbonates (approximately 9%). Furthermore, Sadeghnejad et al. (2023) explores a broader set of parameters, including porosity (11%-15%), specific surface area (ranging from 1.7 to $3.4{\cdot}10^4$), curvature, and Euler characteristics. These studies underscore the complex interplay between porosity, surface area, and heterogeneity, all of which significantly impact fluid flow and permeability in porous media.

Therefore, an analytical relationship would not only improve generalisability but also deepen our understanding of how specific microstructural features influence macroscopic transport properties. In this work, we therefore explore whether permeability can be expressed analytically in terms of MFs. Building on assumptions similar to the classical Kozeny–Carman equation, we derive a new analytical formulation linking MFs to permeability in Sec.3. The model is systematically validated on granular materials represented by random packings of particles, and subsequently applied to cemented microstructures as analogues for carbonate rocks in Sec. 4.

2. Material

2.1. Mathematical description of Minkowski Functionals

To quantitatively describe the microstructure of the porous media, we compute the Minkowski functionals. These functionals offer additive, rotation-invariant, and scale-consistent measures that are especially useful in image-based analysis of porous structures. In this work, we focus on two-dimensional microstructures, where three $(n+1)$

Minkowski functionals are relevant.
The first MF (M_0) corresponds to the body of a volume. Since the goal is to establish a correlation between the MFs and the permeability, the body of interest is the pore space:

$$M_0 = \int_\Omega dV \tag{1}$$

In which V is the pore space. In the analysis, the value is normalised making M_0 equal to the porosity. The second MF (M_1) represents the total interface between the solid and pore space:

$$M_1 = \int_{\delta\Omega} dS \tag{2}$$

In the case of the two-dimensional microstructures, this is equal to the total perimeter of all the solids, which is a measure of length. The third MF (M_2) corresponds to the mean curvature of the sample:

$$M_2 = \int_{\delta\Omega} \left(\frac{1}{r_1} + \frac{1}{r_2} \right) dS \tag{3}$$

However, this is only applicable for higher dimensional microstructures. The fourth MF (M_3) is equal to the Euler Characteristic of the microstructure, expressed as:

$$M_3 = 4\pi\chi\left(\Omega\right) \tag{4}$$

Where $\chi\left(\Omega\right)$ is the Euler characteristic of a solid object. This can be found by the sum of the number of solid particles and cavities, minus the number of redundant loops and results in a quantitative measure. For our samples, the granular material is created in the assumption that the grains are impermeable and have no internal porosity. Therefore, the third MF is equal to the number of particles in the microstructure. For cemented material, the algorithm of van der Walt et al. (2014) is used to define the number of solids, cavities and redundant loops.

2.2. Generated random packings

In order to investigate the general relationship of the MFs with the permeability, we use the samples from a database of microstructures in which the MFs vary independently (Zwarts et al., 2025). In this database, a random packing of circles is generated with PoreSpy (Gostick et al., 2019), controlled by the packing fraction and the random seed. This provides numerous microstructures with a varying M_0. However, since the other Minkowski functionals are directly correlated with M_0 by the properties of the circle, three other grain shapes are inscribed in the circle shape: triangle, rectangle and ellipse. This increases the variance of the different Minkowski functionals which allows for a statistically independent investigation of the contribution of the different Minkowski functionals. Due to the inscription of the various grain shapes in the circles, the condition of non-overlapping grains is preserved. An example of the different random packings is shown in Fig. 1.

To evaluate the influence of anisotropy, packings of rotated shapes are also studied. For each microstructure, a Stokes-flow simulation was performed and the dimensionless permeability was processed following the method of Zwarts and Lesueur (2024a). For

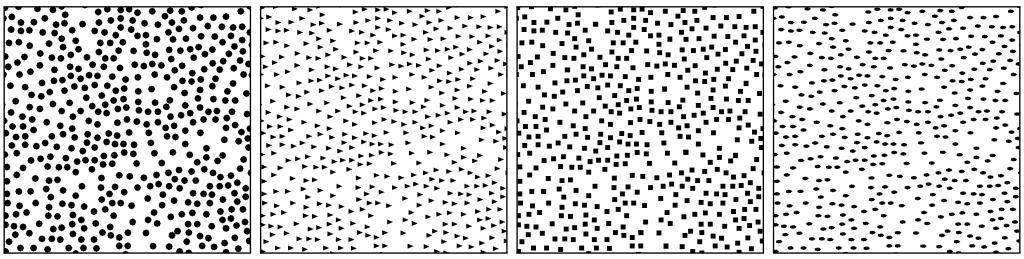

Figure 1: Examples of random packings with a packing fraction of 0.55 for different grain shapes: circle, triangle, rectangle, and ellipse. Grains are shown in black and the pore space in white.

the Representative Elementary Volume convergence, the method of Zwarts and Lesueur (2024b) was followed. 25 samples for each microstructure with the same characteristics (packing fraction, grain shape and grain orientation) were computed, which results in a relative standard deviation of 14.4%. With these samples, we can compute the converged dimensionless permeability.

3. Methods

3.1. Permeability

The analytical derivation of permeability starts from the physical law of Poiseuille, where an incompressible Newtonian laminar flow in a single cylindrical tube with a constant cross section has been shown to be proportional to the dimensions of the tube and the pressure gradient (Sutera and Skalak, 1993). Since the generated dataset consists out of two-dimensional microstructures, the solution of Poiseuille's law is provided in the same dimension:

$$u = \frac{h^2}{12}\frac{\nabla P}{\mu L} \tag{5}$$

In which the h is the diameter (or height) of the cross section, μ is the dynamic viscosity, L is the length of the pipe, and P is the pressure. The solution of the flow is expanded to different shapes of cross-sections, using rectangular, equilateral triangular or elliptical (Boussinesq, 1868) or arbitrary cross-sections (Curle, 1968). However, the flow of a fluid through a porous medium is significantly more complex, as it the path is not equal to the sample length, but includes a tortuous aspect. To account for the hydraulic tortuosity, the length in the equation is replaced with an effective length L_e and the porosity of the cross-section is included.

$$u = \frac{h^2\varepsilon}{12}\frac{L^2}{L_e^2}\frac{\nabla P}{\mu L} = \frac{h^2\varepsilon}{12\tau^2}\frac{\nabla P}{\mu L} \tag{6}$$

In which $\tau = \frac{L_e}{L}$ is the hydraulic tortuosity. This equation can be implemented in Darcy's law to, instead, relate the flow to the permeability of a material:

$$k = \frac{h^2\varepsilon}{12\tau^2} \tag{7}$$

While Poiseuille's law describes the flow in a single cross-section, the flow in a porous medium goes through a complex network of voids. Traditionally, it is assumed that this

network can be simplified by reducing the pore-network to a complex cross-section, which changes the constant 12 of the equation to a coefficient k_s for different shapes (Júnior et al., 2021), similarly to the different solutions of the different cross-sectional shapes. To correlate a general complex cross-section to Poiseuille's law, the hydraulic diameter D_h is introduced, which is equal to four times the ratio of the cross-sectional area of the flow and the wetted perimeter. Instead of the diameter of the tube, this equation is often described with the hydraulic radius m, which correlate in a circular pipe with: $h = 2m$. Once this is combined with Darcy's law (Darcy, 1856), the permeability of the sample can be expressed, and the Kozeny-Carman equation appears:

$$k = \frac{1}{k_s}\frac{1}{\tau^2}\frac{\varepsilon^3}{S^2} \tag{8}$$

Traditionally, the contribution of the tortuosity and shape factor is combined into the empirically derived Kozeny-Carman factor $k_z = k_s\tau^2$, which varies depending on the microstructure of a material. Together with a modified method to describe the surface area based on the average grain size d_p and sphericity of the average grain ϕ_d, a commonly used version of the Kozeny-Carman appears (McCabe et al., 1993). In order to generalise the formulation, we start our derivations from Eq. 7, in which the permeability remains analytically described only in terms of the channel height, porosity and the hydraulic tortuosity.

3.2. Hydraulic Tortuosity

The hydraulic tortuosity is defined as the average path of the path of the fluid divided by the sample length, which we measure for each of the microstructures using PoreSpy. Some studies have shown that there is a correlation between the porosity of the sample and the hydraulic tortuosity. Different types of laws, including natural logarithm (Comiti and Renaud, 1989; Weissberg, 1963; Mauret and Renaud, 1997), roots (Dahlgren and Walker, 1993; Ahmadi et al., 2011; Khabbazi et al., 2016) and power laws (Koponen et al., 1996; Mota et al., 2013) have been proposed. However, we note that the validity of these models significantly depends on the type of microstructure and range of permeability. Nabovati and Sousa (2007) shows that with a stable porosity, the aspect ratio of the grain influences the tortuosity. Therefore, we opt to find a way to predict the permeability based not only on the porosity, but with the MFs to include a full characterisation of the microstructure. We assume that once REV convergence of the different properties has been reached, the permeability does not depend on the geometric distribution of the particles. Therefore, we assume that for a packing where particles are randomly distributed, the average flow path of the fluid in REVs with different geometries is obstructed by the same number of particles, which influences the length of the flow path. The number of obstructions can be estimated by assuming that each of the microstructures can be ideally reorganised in a grid, as shown in Fig. 2, without changing its hydraulic properties. A comparison of this is shown in Appendix A.

From the schematic, it is evident that the average flow path can be divided into two sections: a free path L and an obstructed path L_o. In random packings of non-overlapping grains without cavities, the total number of particles equals Euler's characteristic M_3, which implies that the number of grains interfering with one obstructed flow path in length is proportional to $\sqrt{M_3}$. The perimeter of a single particle can be determined by

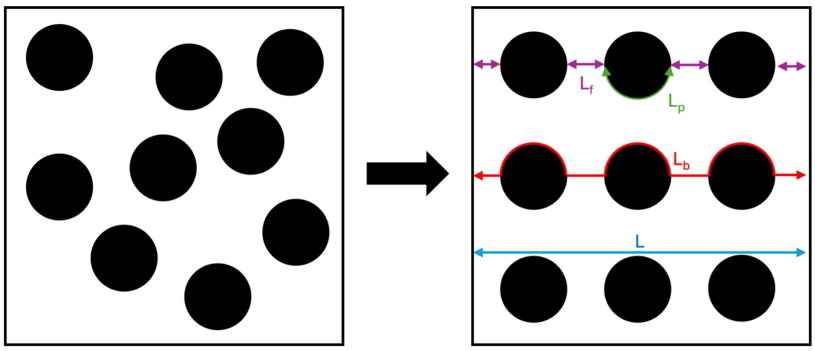

Figure 2: Schematic of the reorganisation of the grains from the random packing into a uniform grid of equal packing fraction. The red line provides an estimation of the tortuous flow path and the blue arrow shows the undisturbed flow path.

dividing the total surface area M_1 by Euler's characteristic M_3. In the schematics, half of the particle's perimeter is considered part of the obstructed path. However, the tortuous flow does not strictly follow this half-perimeter; instead, it takes a smoother trajectory around the particle. To account for this, an optional coefficient c_1 is introduced in the general formulation, resulting in the length per particle contribution L_p to the obstructed path:

$$L_p = \sqrt{M_3}\frac{M_1}{c_1 M_3} \tag{9}$$

To provide an estimate of the empty spaces in between each particle, we assume that we can derive an equivalent diameter of each particle, by dividing the perimeter of the induvial particle with π (which returns the input parameter of the circle diameter for the circular packing) and extract the sum of the diameters L_d from the total length. As with the particles, the number of channels is approximated with $\sqrt{M_3}$. Combining all leads to the following formulation of the obstructed path:

$$L_o = L_p + L_f = L_p + (L - L_d) = \frac{M_1}{c_1\sqrt{M_3}} + \left(L - \frac{M_1}{\pi\sqrt{M_3}}\right) \tag{10}$$

The free flow path is non-obstructed and therefore equal to the sample length (L). The hydraulic tortuosity is estimated with the weighted average of the obstructed and free path, leading to the following formulation of the tortuosity based on the MFs:

$$\tau = \frac{L_o L_d + L L_f}{L_d + L_f} \tag{11}$$

Which results after simplification in the following formulation of τ:

$$\tau = 1 + \frac{M_1^2}{\pi M_3}\left(\frac{1}{c_1} - \frac{1}{\pi}\right) \tag{12}$$

Based on the schematics of A.14, the effective flow path follows the boundary of the shape, and therefore the contribution of c_1 is equal to exactly 2.0. In reality, the effective flow path around a grain is generally slightly longer than half of the perimeter. In

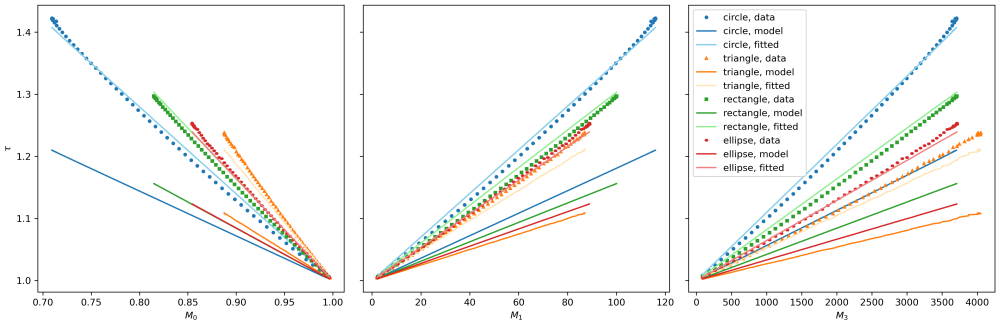

Figure 3: The comparison between the simulated dimensionless tortuosity values (shown with markers) and the predictions from Eq. 12 (shown with continuous lines) across a range of packing fractions. The data is plotted against different MFs (M_0 on the left, M_1 in the middle and M_3 on the right) to assess their correlation with tortuosity. The different colours, with matching markers to the particle shape, indicate the grain shape within the packing (blue = circle, orange = triangle, green = rectangle, red = ellipse). In this comparison, the orientation of the grains is randomly distributed throughout the random packing.

addition, the weighted averaging of obstructed and free flow paths influences this contribution. As a first approximation, we therefore set the coefficient $c_1 = 2.0$, corresponding to exactly half the perimeter of a grain. To refine this estimate and test the validity of the formulation, we calibrate c_1 using the tortuosity of the circle packing. This fitting procedure yields $c_1 = 1.5$, which is subsequently applied across the other microstructures. The predicted tortuosities based on this calibrated value are presented in Fig. 3.

Equation 12 captures the general trend of the measured hydraulic tortuosity: τ decreases with M_0 and increases with M_1 and M_2. Using the initial assumption of $c_1 = 2.0$ systematically underestimates tortuosity, whereas the fitted value $c_1 = 1.5$ yields much better agreement across grain shapes. For circular and ellipsoidal grains, the calibrated model reproduces the simulated tortuosities particularly well. In contrast, triangular grains show small growing deviations at lower porosities, indicating that the current assumption for fitting —that the path length is only slightly greater than half the grain perimeter— does still not fully capture the influence of sharp particle edges. For rectangles, such deviations are less pronounced due to the more symmetric geometry of the randomly generated packings. For completeness, the fitted c_1 values for the rectangle and ellipse packings both result in 1.5, whereas the c_1 value for triangles results in 1.4, respectively.

The proposed method is compared against established tortuosity models from Koponen et al. (1996, 1997); Matyka et al. (2008); Weissberg (1963), as shown in Fig. 4. Overall, the MF-based formulation, with a single calibrated parameter, reproduces the simulated tortuosities with good accuracy across all grain shapes. While the model of Koponen et al. (1996) provides slightly better agreement for random packings of triangles, the MF-based approach captures the general trend within a unified framework, demonstrating both its robustness and versatility.

It is important to note that Minkowski functionals are motion-invariant and therefore do not account for anisotropy. To explore the role of anisotropy in tortuosity estimation, we computed τ for packings where grains were uniformly aligned in different orientations:

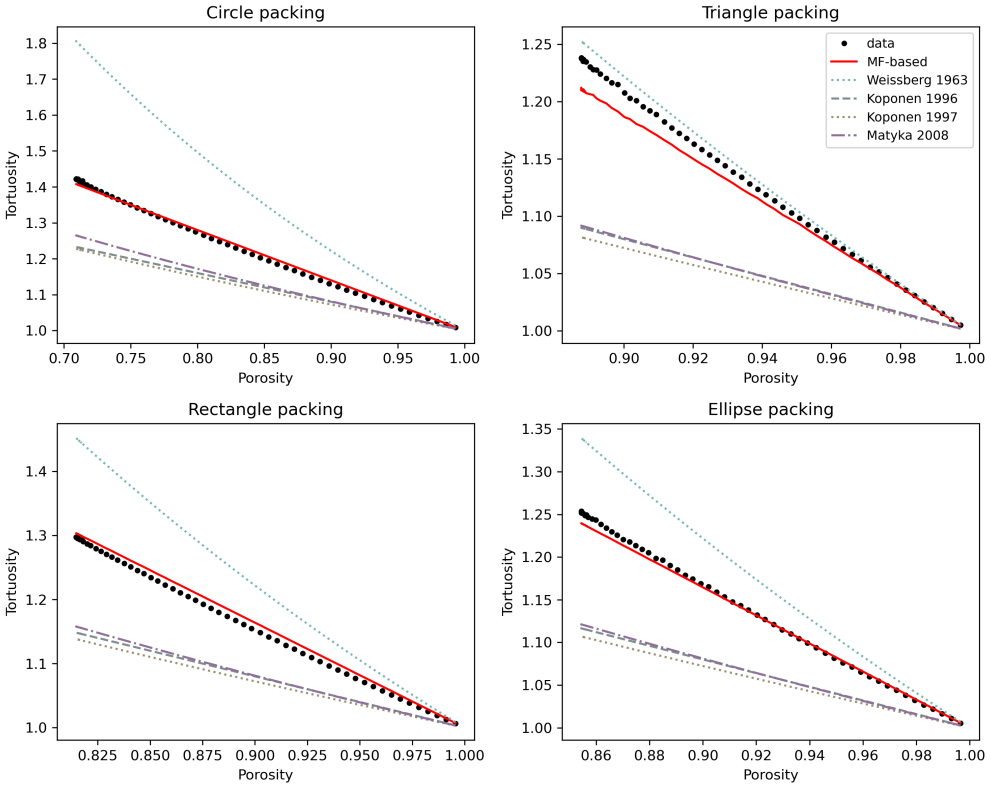

Figure 4: Comparison between simulated tortuosity values (markers) and predictions from the MF-based model (continuous black lines) and established correlations from Koponen et al. (1996, 1997); Matyka et al. (2008); Weissberg (1963) (colored lines). Results are shown for random packings of different grain shapes.

parallel, diagonal, and perpendicular to the flow. The results of the tortuosity predicted by the model, excluding the unaffected circle packing, are shown in Fig. 5.

As expected, anisotropy is not captured in the current formulation: for ellipsoidal and triangular grains, the predicted values consistently over- or underestimate the simulations depending on orientation. Although the mismatch is systematic, as the alignment parallel to the flow seems to underestimate the tortuosity and the perpendicular orientation overestimates the tortuosity, it highlights the need for directional parameters in the tortuosity formulation if anisotropic effects are to be accounted for. Orientation of the rectangular grain shape, obviously, is not affected by the 90° rotation. We observe a slight overestimation of the tortuosity, when we compare it to the randomly distributed rectangular random packing. Together with the over- and underestimation of the ellipsoid and triangular random packings, we conclude that even though the prediction might be fairly accurate for random orientations, the flow path through the structured grain shape orientation is difficult to capture with the current estimation.

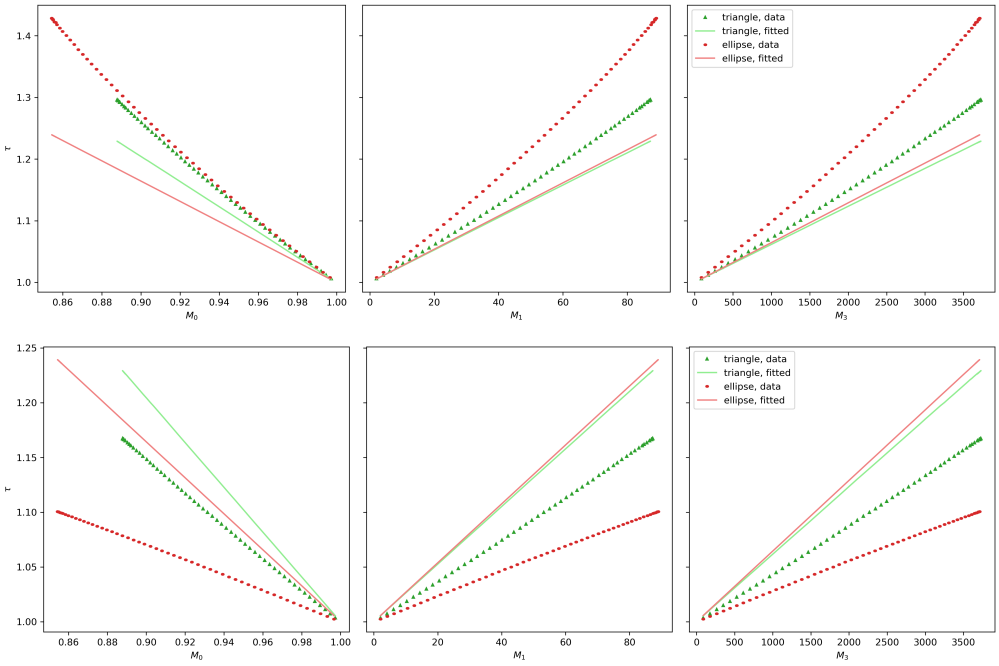

Figure 5: Comparison between simulated tortuosity values (markers) and predictions from Eq. 12 (continuous lines) shown against three different MFs (left: M_0, middle: M_1, right: M_3). Again, the different colours indicate the different grain shapes within the random packing (green = triangles, red = ellipses). In the top row, the grains are orientated in the direction of the flow, meaning the triangles are pointing in the flow direction and the major axis of the ellipses is equal to the flow direction. The bottom row shows the results for a 90° rotation, perpendicular to the flow direction. The triangles are pointing upwards and the minor axis of the ellipses is aligned to the flow direction.

3.3. Shape factor

The other unknown in Eq. 7 is the effective pore size that represents the void geometry. The method of Kozeny-Carman assumes that a void network can be represented as a complex cross-section and introduces the hydraulic radius and a shape factor c_s to generalise this part in the formulation. This shape factor is a variable which has to be calibrated for each different microstructure and is shown to vary significantly. Where Kozeny-Carman estimate the constant to be around 5 (Carman, 1939), higher values of over 130 are found for real microstructures (Mostaghimi et al., 2012). Instead, we follow on the assumption that the flow through the network of voids can be represented as a channel, but approach it with an effective height of the channel, keeping closer to the formulation of Poiseuille. The schematic shown in Fig. 2 and the assumption that the hydraulic properties are independent of the exact geometry once REV convergence has been achieved, lead to a rough estimation of the channel width as: $h_{ef} = \frac{M_0}{\sqrt{M_3}}$. The coefficient in the denominator originates from the analytical solution of the governing differential equation and, as such, depends on both the geometry and dimensionality of the flow channel. Because this coefficient is shape-dependent, further refinements could be pursued by adjusting the shape factor. To account for this, we introduce a second

coefficient, c_2, initially set to 12 matching Poiseuille's tube, which—together with the channel height—defines a generalised shape factor:

$$c_s = \frac{h_{ef}^2}{c_2} = \frac{M_0^2}{c_2 M_3} \tag{13}$$

With the tortuosity, porosity and permeability known from simulations on the random packings, the channel height can be isolated, which allows us to compare the estimated values with the computed values, as shown in Fig. 6. As with the tortuosity, we also fit the parameter c_2 to the circle packing, which results in a value of 15, and use that for the other packings as well.

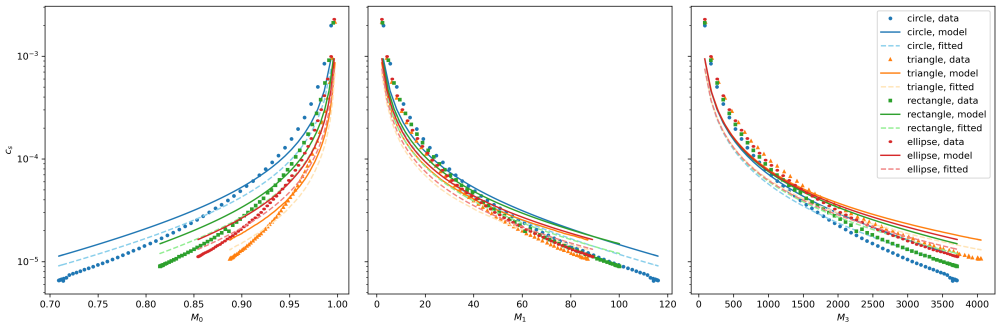

Figure 6: The comparison of the shape factor c_s of the computed and estimated values, shown with respect to the MFs (left: M_0, middle: M_1, right: M_3).

We observe that the shape factor increases exponentially with porosity, while it decreases exponentially with both surface area and the Euler characteristic. The simple channel estimate from Eq. 13 reproduces these overall trends reasonably well but tends to overestimate the exponential slope at lower porosities. This behaviour is consistent across all grain shapes, though the deviations become more pronounced for triangular grains. Introducing the fitted parameter from the circle packing improves the predictions at low porosity for all shapes, but at higher porosities, we observe a slightly extra underestimation of the shape factor.

The observation that the differnt grain rougness influence the is equivalently confirmed when different grain orientations are considered, as shown in Fig. 7. For grains rotated perpendicular to the flow direction (90°), the shape factor is strongly underestimated, reflecting the reduced channel width in this configuration. In contrast, for randomly oriented packings, the predictions align more closely, particularly for elliptical grains. These results indicate that a perfect correlation requires incorporating directional information into the Minkowski functionals formulation. Nevertheless, for random packings with uniformly distributed grain orientations, the isotropic nature of the Minkowski functionals appears to provide a sufficient approximation.

3.4. Permeability

With an estimation of the hydraulic tortuosity and the contribution of the channel, all the parameters of Eq. 7 can be expressed in terms of the MFs. Both τ and c_s expressed

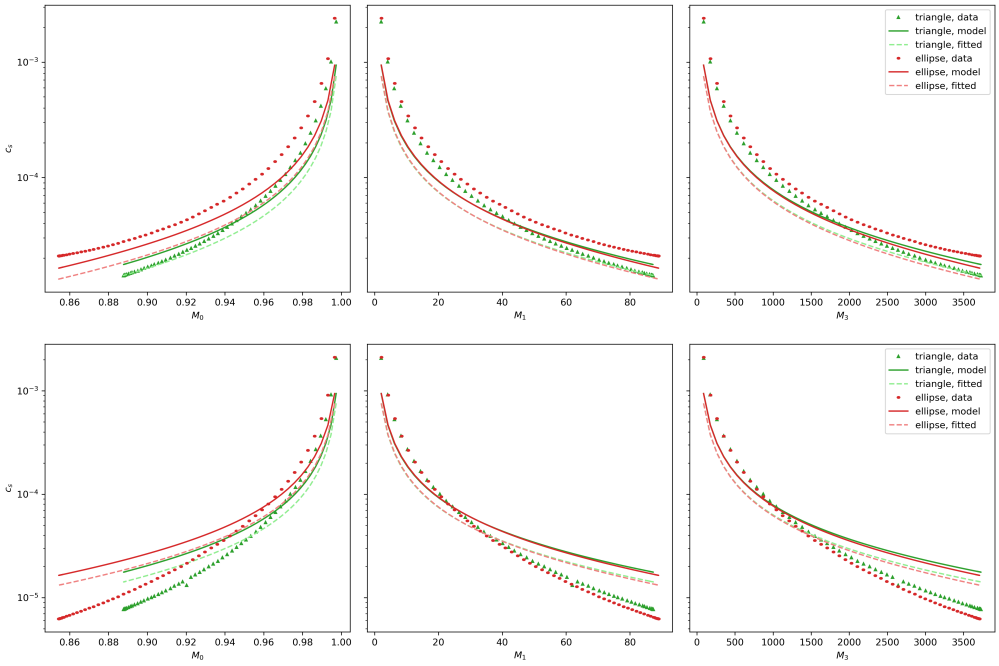

Figure 7: Comparison between the simulated shape factor (shown as markers) and the predictions from Eq. 13 (dashed lines) across a range of packing fractions. The data is plotted against various Minkowski functionals. Different colours represent different grain shapes, each uniformly aligned at a fixed angle throughout the packing. The top row shows the results of the tortuosity with the grains aligned with the direction of the flow, and the bottom row shows the results when the grains are perpendicular to the flow.

in MFs, leads to the following formulation of the permeability:

$$k = \frac{M_0^3}{c_2 M_3 \left(1 + \frac{M_1^2}{M_3 \pi}\left(\frac{1}{c_1} + \frac{1}{\pi}\right)\right)} \tag{14}$$

We first compare the permeability of circle packings, as shown in Fig. 8. The results are shown with the permeability on log-scale to highlight the differences between the extreme values. For validation purposes, the Kozeny-Carman prediction of the permeability is included, for which the shape constant is fitted on the circular packing. As can be observed, the general trend of the permeability is captured by the model based on the MFs, although the prediction slightly overestimates the permeability with lower porosities and underestimates the permeability with higher porosities. These deviations can be related to the shape factor, which presents similar trends in earlier results. For the permeability prediction based on MFs, it was assumed to take only a part of the grain boundary into account when determining the tortuosity and it is clear that the estimation of the equivalent channel height is unrefined, due to the complexity of the void space. Therefore, the coefficient of the shape factor is fitted to the data, which results in the same underestimation with higher porosities, but a near-perfect match on

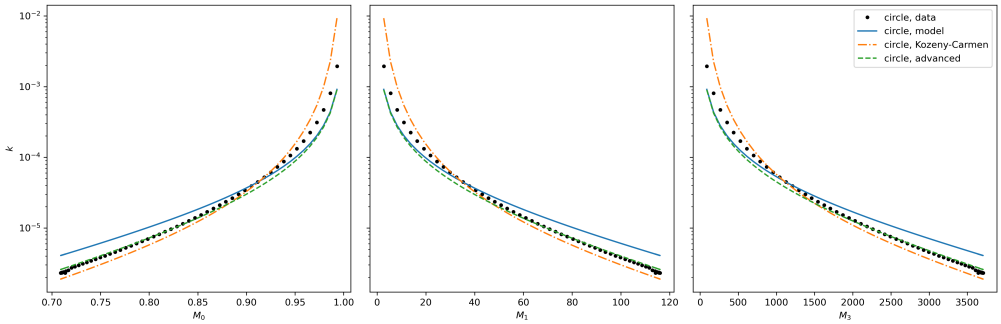

Figure 8: The comparison of the permeability of the circle packing, shown with respect to M_0 (left), M_1 (middle) and M_3 (right). The simulated data is shown with black markers. The estimation based on the MFs is shown in the continuous blue line. The prediction of the permeability with Kozeny-Carmen is shown in an orange dash-dot line and advanced version of the MFs model is shown in a green dashed line.

the lower porosities. This indicates that there is a direct correlation between the MFs and the permeability in motion invariant samples, although better assumptions could be made in the approximation of the tortuosity and the shape factor. Compared to the Kozeny-Carman standard, the prediction of the permeability with MFs performs very similar, and even better when the results are fitted. The results are extended to the random packings with different grain shapes, as shown in Fig. 9. For consistency in the

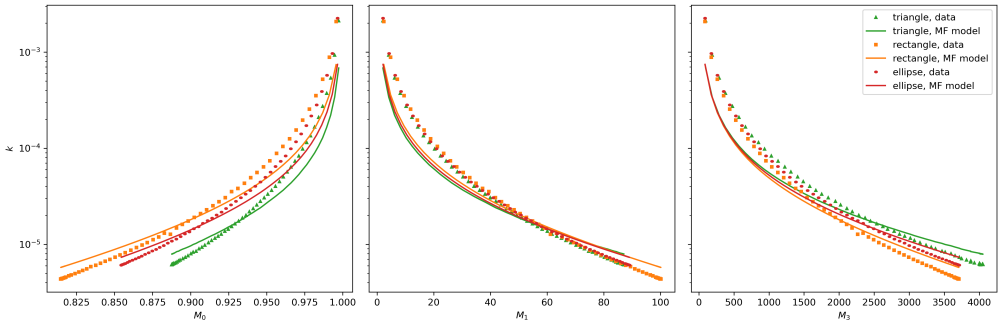

Figure 9: The comparison of the dimensionless permeability of the different grain shapes in the random packings. The data is shown with markers with a linked colour to the different grain shapes, MF model with a continuous line and the same colour as the markers.

Kozeny-Carman comparison, the previously fitted value of the shape factor is used for the different particle shapes. We observe that for each of the different grain shapes, similar trends can be found: The MFs model shows a slight overestimation with lower porosities, but underestimation with higher porosities. Similarly, for the fitted models, the prediction remains slightly underestimated when dealing with high porosities but reaches very accurate predictions with lower porosities, despite using a fitting coefficient calibrated on the circle packings.

4. Cemented microstructures

To predict permeability from MFs, we previously assumed that each grain can be distinguished individually, allowing the Euler characteristic to be directly related to obstacles in the flow path. However, natural porous media often consist of cemented grains forming a continuous rock matrix with complex, and not always fully connected, void geometries. In such systems, the pore space resembles an interconnected channel network rather than discrete grain separations. This alters both the microstructural characteristics captured by the MFs—no longer linearly related to each other—and the fluid flow behaviour. Previous work by Sadeghnejad et al. (2023) demonstrated that in cemented systems, the Euler characteristic can even become negative, indicating poor connectivity in the void space, a feature absent in granular packings of impermeable particles.

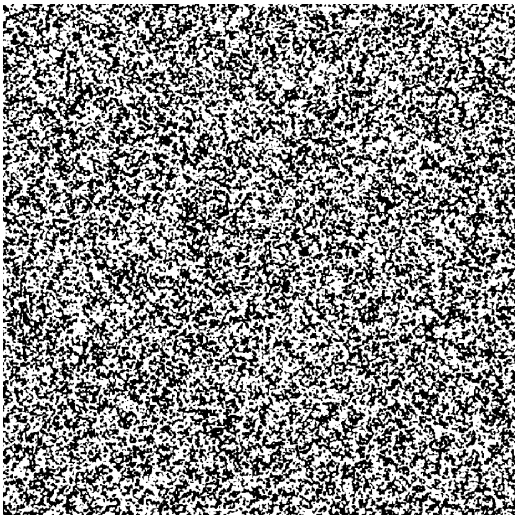

Figure 10: An example of a cemented microstructure with a porosity of 55% and a blobiness of 15.0. The white colour represents the rock matrix and the black represents the void space.

To investigate this behaviour, we use different samples from the dataset of Zwarts et al. (2025). Those were generated using the blob generator described by Gostick et al. (2019). This approach applies Gaussian blurring to random noise to produce binary images with cemented morphologies. This produces samples with resembling features of some carbonate rocks. Samples were generated with varying porosity (55–95% in steps of 4.5%) and the "blobiness" parameter (1–15 in steps of 1). For each sample, permeability, tortuosity, and MFs were computed using the same methodology as for the granular packings. Figure 11 compares measured tortuosity with predictions based on MFs for blobiness = 15.

Figure 11 shows that tortuosity exhibits an exponential decay with respect to M_0, an exponential increase with respect to M_1, and an S-shaped relation with M_3. These behaviours differ markedly from the granular packings. Moreover, the tortuosity values in cemented materials range from 1 up to over 17, compared to values below 1.5 for granular packings. The MF-based predictions reproduce the qualitative trends but underestimate

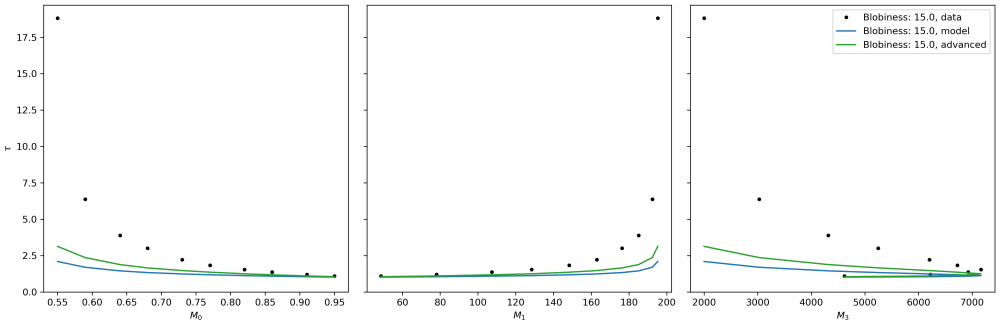

Figure 11: The hydraulic tortuosity of cemented microstructures with a blobiness of 15, varying in porosity from 55% up to 95%, shown with respect to M_0 (left), M_1 (middle) and M_3 (right). The measured values are shown with markers, whereas the prediction based on MFs is shown with a continuous line.

the magnitude, particularly at low porosities. Using the calibrated value of $c_1 = 1.49$ from the circular packings improves accuracy but remains insufficient. Direct fitting of c_1 to the cemented data yields values between 0.36 and 0.63, indicating that the current treatment of the Euler characteristic in the tortuosity model requires refinement for low-porosity cemented media, which deviate more strongly from the assumptions underlying the model. Fig. 12 shows the comparison of the shape factor predicted by the model with the measured values.

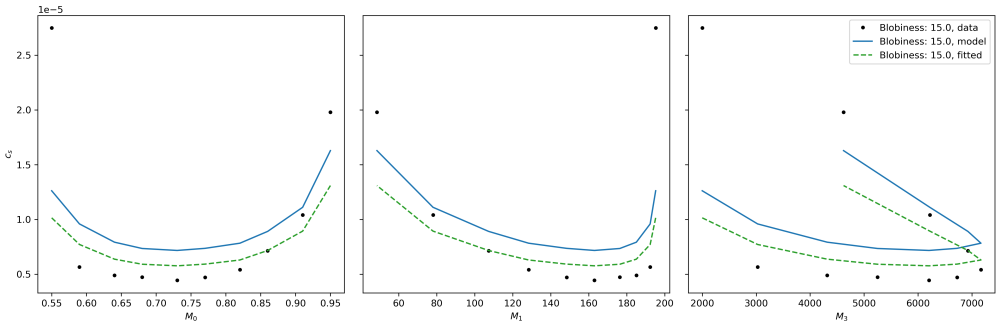

Figure 12: The shape factor of cemented microstructures with a blobiness of 15, varying in porosity from 55% up to 95%, shown with respect to M_0 (left), M_1 (middle) and M_3 (right). The measured values are shown with markers, whereas the prediction based on MFs is shown with a continuous line.

In contrast to the granular packings, where exponential relations were observed, the cemented microstructures display a distorted U-shaped trend. Despite the highly non-linear relation, the MF-based predictions reproduce the overall trend but still deviate in magnitude, indicating that the current formulation does not fully capture the effect of cementation on the shape factor. However, when the model is with the fitted coefficient from the circle packing, the agreement improves considerably in both shape and value, suggesting a strong but non-trivial link between MFs and permeability in cemented systems. Notably, the fitted values of c_2 rise drastically, reaching values up to 140, consistent with the large variations in the Kozeny–Carman coefficient reported by Mostaghimi et al.

(2012). Combining the tortuosity and shape factor estimations, we extend the analysis to permeability predictions for cemented microstructures, as shown in Fig. 13. Compared to granular packings, dimensionless permeability values are significantly lower, spanning 10^{-8} to 10^{-5}, while granular systems ranged from 10^{-5} to 10^{-2}. Furthermore, the relationship with MFs differs qualitatively. In granular systems, permeability increased exponentially with porosity, decreased with increasing M_1, and increased with decreasing M_3. In cemented systems, permeability follows a more complex trend: stabilising and then decreasing with M_1 and showing an inverted relationship with M_3.

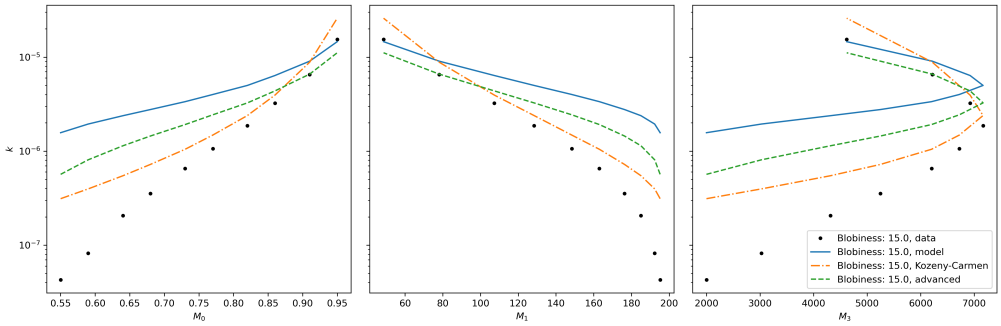

Figure 13: The permeability of the cemented microstructure. The simulated data is shown with markers, the model based on MFs is shown in a continuous line, the Kozeny-Carman prediction is shown with a dash-dot line in dark blue and the improved model with the dashed line and light blue colour.

The MF-based model (continuous line) captures the overall trends but systematically overestimates the absolute values, with deviations exceeding an order of magnitude. The Kozeny–Carman model with parameters fitted to circular packings exhibits similar discrepancies. The pronounced mismatch at low permeabilities correlates with the large tortuosity deviations, reflecting the limitation of assuming that obstacles can be directly described by M_3. To test whether restricting the analysis to accessible pore space improves predictions, we also computed effective MFs. However, no improvement was observed, indicating that refinements in the treatment of tortuosity or the Euler characteristic are necessary to achieve more accurate permeability predictions in cemented morphologies.

5. Conclusion

In this work, we examine whether Minkowski functionals (MFs) can serve as sufficient geometrical descriptors to predict permeability in both granular and cemented microstructures. Using image-based analyses, we compute MFs from synthetic microstructures and extract hydraulic properties via postprocessed Stokes-flow simulations. Based on the approximation of a granular material reorganisation into a uniform grid, we analytically derive permeability in terms of an effective channel width and the tortuosity of the medium. Assuming that the hydraulic properties (e.g. permeability and tortuosity) and MFs (porosity, surface area, Euler characteristic) have converged at the REV scale, we derive a predictive equation for permeability based solely on MFs.

For granular packings, the MF-based model captures the variation of permeability across

a large range of porosities and particle shapes. Systematic deviations remain — with slight overestimation at low porosity and underestimation at high porosity — but a single calibration of the shape coefficient using circular grains substantially improves accuracy and generalises well across triangle, rectangle, and ellipse packings. With this calibration, the model reproduces measured permeability in good agreement, achieving performance comparable to the classical Kozeny–Carman formulation.

For cemented microstructures, the situation is more complex. Tortuosity spans a much wider range (up to 17), and the shape factor shows a distorted U-shaped dependence on the MFs. While the MF-based model captures qualitative trends with M_0, M_1, and M_3, it underestimates permeability magnitude, especially at low porosity, offering a performance level similar to Kozeny–Carman while relying on more general morphological descriptors. The underestimation points to the need for improved treatment of connectivity and constrictions. Importantly, direct fitting to the cemented dataset still yields good agreement, reinforcing the predictive value of MFs even in structurally rigid systems.

The impact of anisotropy was also examined in samples with oriented grains (aligned, perpendicular, and diagonal to the flow). While permeability is sensitive to orientation, MFs are motion-invariant and therefore unable to capture this directional dependence. This limitation highlights the potential of extending the framework with directional morphological descriptors, such as Minkowski tensors, which can address anisotropy in porous media (Nair et al., 2021; Zhang et al., 2025).

Overall, our results demonstrate that MFs provide a compact and versatile framework for predicting permeability directly from microstructural geometry. Beyond granular and cemented media, such formulations offer a pathway toward analytical, generalised models that bridge morphology and physical properties.

Bibliography

Ahmadi, M.M., Mohammadi, S., Hayati, A.N., 2011. Analytical derivation of tortuosity and permeability of monosized spheres: A volume averaging approach. Physical Review E—Statistical, Nonlinear, and Soft Matter Physics 83, 026312.

Armstrong, R.T., McClure, J.E., Robins, V., Liu, Z., Arns, C.H., Schlüter, S., Berg, S., 2018. Porous media characterization using minkowski functionals: Theories, applications and future directions. Transport in Porous Media 130, 305–335. doi:10.1007/s11242-018-1201-4.

Bear, J., 1972. Dynamics of fluids in porous media. Courier Corporation.

Boussinesq, J., 1868. Théorie nouvelle des ondes lumineuses. J. Mathématiques Pures et Appliquées 2, 313–339.

Carman, P.C., 1939. Permeability of saturated sands, soils and clays. The Journal of Agricultural Science 29, 262–273. URL: https://www.cambridge.org/core/product/identifier/S0021859600051789/type/journal_article, doi:10.1017/S0021859600051789.

Chapuis, R.P., Aubertin, M., 2003. On the use of the kozeny-carman equation to predict the hydraulic conductivity of soils. Canadian Geotechnical Journal 40, 616–628. doi:10.1139/t03-013.

Comiti, J., Renaud, M., 1989. A new model for determining mean structure parameters of fixed beds from pressure drop measurements: application to beds packed with parallelepipedal particles. Chemical Engineering Science 44, 1539–1545. doi:10.1016/0009-2509(89)80031-4.

Curle, N., 1968. Modern fluid dynamics. Van Nostrand Reinhold.

Dahlgren, R.A., Walker, W.J., 1993. Aluminum release rates from selected spodosol bs horizons: Effect of ph and solid-phase aluminum pools. Geochimica et Cosmochimica Acta 57, 57–66. doi:10.1016/0016-7037(93)90468-c.

Darcy, H., 1856. Les fontaines publiques de Dijon.

Gostick, J., Khan, Z., Tranter, T., Kok, M., Agnaou, M., Sadeghi, M., Jervis, R., 2019. Porespy: A python toolkit for quantitative analysis of porous media images. Journal of Open Source Software 4, 1296. doi:10.21105/joss.01296.

Heijs, A.W.J., Lowe, C.P., 1995. Numerical evaluation of the permeability and the kozeny constant for two types of porous media. Physical Review E 51, 4346–4352. doi:10.1103/physreve.51.4346.

Hommel, J., Coltman, E., Class, H., 2018. Porosity–permeability relations for evolving pore space: A review with a focus on (bio-)geochemically altered porous media. Transport in Porous Media 124, 589–629. doi:10.1007/s11242-018-1086-2.

Hu, W., Dano, C., Hicher, P.Y., Le Touzo, J.Y., Derkx, F., Merliot, E., 2011. Effect of sample size on the behavior of granular materials. Geotechnical Testing Journal 34, 186–197. doi:10.1520/gtj103095.

Hu, Y., Wang, Q., Zhao, J., Xie, S., Jiang, H., 2020. A novel porous media permeability model based on fractal theory and ideal particle pore-space geometry assumption. Energies 13, 510. doi:10.3390/en13030510.

Jones, M., Clarke, N., 2021. Machine learning real space microstructure characteristics from scattering data. Soft Matter 17, 9689–9696. doi:10.1039/d1sm00818h.

Júnior, V.A.S., Júnior, A.F.S., Simões, T.A., Oliveira, G.P., 2021. Poiseuille-number-based kozeny–carman model for computation of pore shape factors on arbitrary cross sections. Transport in Porous Media 138, 99–131. doi:10.1007/s11242-021-01592-4.

Kazemi, H., Merrill, L., Porterfield, K., Zeman, P., 1976. Numerical simulation of water-oil flow in naturally fractured reservoirs. Society of Petroleum Engineers Journal 16, 317–326. doi:10.2118/5719-pa.

Khabbazi, A.E., Hinebaugh, J., Bazylak, A., 2016. Determining the impact of rectangular grain aspect ratio on tortuosity–porosity correlations of two-dimensional stochastically generated porous media. Science Bulletin 61, 601–611. URL: https://linkinghub.elsevier.com/retrieve/pii/S2095927316301414, doi:10.1007/s11434-016-1020-3.

Koponen, A., Kataja, M., Timonen, J., 1996. Tortuous flow in porous media. Phys. Rev. E 54, 406–410. URL: https://link.aps.org/doi/10.1103/PhysRevE.54.406, doi:10.1103/PhysRevE.54.406.

Koponen, A., Kataja, M., Timonen, J., 1997. Permeability and effective porosity of porous media. Physical Review E 56, 3319–3325. doi:10.1103/physreve.56.3319.

Lei, G., Liu, T., Liao, Q., He, X., 2023. Estimating permeability of porous media from 2d digital images. Journal of Marine Science and Engineering 11, 1614. doi:10.3390/jmse11081614.

Li, B., Wong, R.C., Heidari, S., 2018. A modified kozeny-carman model for estimating anisotropic permeability of soft mudrocks. Marine and Petroleum Geology 98, 356–368. doi:10.1016/j.marpetgeo.2018.08.034.

Li, P.N., Xu, Y.S., Wang, X.W., 2023. Estimation of hydraulic conductivity by the modified kozeny–carman equation considering the derivation principle of the original equation. Journal of Hydrology 621, 129658. doi:10.1016/j.jhydrol.2023.129658.

Lindqwister, W., Peloquin, J., Dalton, L.E., Gall, K., Veveakis, M., 2025. Predicting compressive stress-strain behavior of elasto-plastic porous media via morphology-informed neural networks. Communications Engineering 4. doi:10.1038/s44172-025-00410-9.

Liu, Y., Jeng, D.S., 2019. Pore scale study of the influence of particle geometry on soil permeability. Advances in Water Resources 129, 232–249. doi:10.1016/j.advwatres.2019.05.024.

Matyka, M., Khalili, A., Koza, Z., 2008. Tortuosity-porosity relation in porous media flow. Physical Review E 78, 026306. doi:10.1103/physreve.78.026306.

Mauret, E., Renaud, M., 1997. Transport phenomena in multi-particle systems—i. limits of applicability of capillary model in high voidage beds-application to fixed beds of fibers and fluidized beds of spheres. Chemical Engineering Science 52, 1807–1817. doi:10.1016/s0009-2509(96)00499-x.

McCabe, W.L., Smith, J.C., Harriott, P., 1967. Unit operations of chemical engineering. volume 5. McGraw-hill New York.

McCabe, W.L., Smith, J.C., Harriott, P., 1993. Unit operations of chemical engineering. McGraw-hill.

Mostaghimi, P., Blunt, M.J., Bijeljic, B., 2012. Computations of absolute permeability on micro-ct images. Mathematical Geosciences 45, 103–125. doi:10.1007/s11004-012-9431-4.

Mota, M., Yelshin, A., Yelshina, I., 2013. Porous media in biotechnology. Downstream Industrial Biotechnology: Recovery and Purification , 277.

Nabovati, A., Sousa, A.C.M., 2007. Fluid Flow Simulation in Random Porous Media at Pore Level Using Lattice Boltzmann Method. Springer Berlin Heidelberg. pp. 518–521. doi:10.1007/978-3-540-75995-9_172.

Nair, P., Mühlbauer, S., Roy, S., Pöschel, T., 2021. Can minkowski tensors of a simply connected porous microstructure characterize its permeability? Physics of Fluids 33. doi:10.1063/5.0045701.

Nomura, S., Yamamoto, Y., Sakaguchi, H., 2018. Modified expression of Kozeny–Carman equation based on semilog–sigmoid function. Soils and Foundations 58, 1350–1357. URL: https://linkinghub.elsevier.com/retrieve/pii/S0038080618301896, doi:10.1016/j.sandf.2018.07.011.

Nooruddin, H.A., Hossain, M.E., 2011. Modified kozeny–carmen correlation for enhanced hydraulic flow unit characterization. Journal of Petroleum Science and Engineering 80, 107–115. doi:10.1016/j.petrol.2011.11.003.

Panda, M.N., Lake, L.W., 1994. Estimation of single-phase permeability from parameters of particle-size distribution. AAPG bulletin 78, 1028–1039.

Peaceman, D., 1976. Convection in fractured reservoirs - the effect of matrix-fissure transfer on the instability of a density inversion in a vertical fissure. Society of Petroleum Engineers Journal 16, 269–280. doi:10.2118/5523-pa.

Sadeghnejad, S., Reinhardt, M., Enzmann, F., Arnold, P., Brandstätter, B., Ott, H., Wilde, F., Hupfer, S., Schäfer, T., Kersten, M., 2023. Minkowski functional evaluation of representative elementary volume of rock microtomography images at multiple resolutions. Advances in Water Resources 179, 104501. URL: https://linkinghub.elsevier.com/retrieve/pii/S0309170823001367, doi:10.1016/j.advwatres.2023.104501.

Safari, M., Gholami, R., Jami, M., Ananthan, M.A., Rahimi, A., Khur, W.S., 2021. Developing a porosity-permeability relationship for ellipsoidal grains: A correction shape factor for kozeny-carman's equation. Journal of Petroleum Science and Engineering 205, 108896. doi:10.1016/j.petrol.2021.108896.

Santaló, L.A., Kac, M., 2004. Integral Geometry and Geometric Probability. Cambridge University Press. doi:10.1017/cbo9780511617331.

Schepp, L.L., Ahrens, B., Balcewicz, M., Duda, M., Nehler, M., Osorno, M., Uribe, D., Steeb, H., Nigon, B., Stöckhert, F., Swanson, D.A., Siegert, M., Gurris, M., Saenger, E.H., 2020. Digital rock physics and laboratory considerations on a high-porosity volcanic rock. Scientific Reports 10. doi:10.1038/s41598-020-62741-1.

Schneider, R., 2014. Convex bodies. Number 151 in Encyclopedia of mathematics and its applications. 2nd expanded edition ed., Cambridge Univ. Press, Cambridge.

Slotte, P.A., Berg, C.F., Khanamiri, H.H., 2020. Predicting Resistivity and Permeability of Porous Media Using Minkowski Functionals. Transport in Porous Media 131, 705–722. URL: http://link.springer.com/10.1007/s11242-019-01363-2, doi:10.1007/s11242-019-01363-2.

Sutera, S.P., Skalak, R., 1993. The History of Poiseuille's Law. Annual Review of Fluid Mechanics 25, 1–20. URL: https://www.annualreviews.org/doi/10.1146/annurev.fl.25.010193.000245, doi:10.1146/annurev.fl.25.010193.000245.

de Swaan, A., 1990. Influence of shape and skin of matrix-rock blocks on pressure transients in fractured reservoirs. SPE Formation Evaluation 5, 344–352. doi:10.2118/15637-pa.

Torskaya, T., Shabro, V., Torres-Verdín, C., Salazar-Tio, R., Revil, A., 2014. Grain Shape Effects on Permeability, Formation Factor, and Capillary Pressure from Pore-Scale Modeling. Transport in Porous Media 102, 71–90. URL: http://link.springer.com/10.1007/s11242-013-0262-7, doi:10.1007/s11242-013-0262-7.

van der Walt, S., Schönberger, J.L., Nunez-Iglesias, J., Boulogne, F., Warner, J.D., Yager, N., Gouillart, E., Yu, T., the scikit-image contributors, 2014. scikit-image: image processing in python. PeerJ 2, e453. doi:10.7717/peerj.453.

Weissberg, H.L., 1963. Effective diffusion coefficient in porous media. Journal of Applied Physics 34, 2636–2639. doi:10.1063/1.1729783.

Witherspoon, P.A., Wang, J.S.Y., Iwai, K., Gale, J.E., 1980. Validity of cubic law for fluid flow in a deformable rock fracture. Water Resources Research 16, 1016–1024. doi:10.1029/wr016i006p01016.

Yazdchi, K., Srivastava, S., Luding, S., 2011. On the validity of the carman-kozeny equation in random fibrous media, in: 2nd International Conference on Particle-based Methods, PARTICLES 2011, Eccomas. pp. 1–10.

Ye, Y., Xu, Z., Zhu, G., Cao, C., 2022. A modification of the kozeny–carman equation based on soil particle size distribution. Arabian Journal of Geosciences 15. doi:10.1007/s12517-022-10224-0.

Zhang, Z., Li, C., Ye, Y., Lu, S., 2025. Rank-two tensorial shape descriptors: Insights into anisotropic permeability tensor characterization. Physics of Fluids 37. doi:10.1063/5.0249824.

Zhong, Y., Zhou, A., Du, J., Teng, J., Shen, S.l., 2023. Modified kozeny-carman equation for estimating hydraulic conductivity in nanoscale pores of clayey soils with active surfaces. Journal of Hydrology 626, 130209. doi:10.1016/j.jhydrol.2023.130209.

Zubov, A.S., Khlyupin, A.N., Karsanina, M.V., Gerke, K.M., 2024. In search for representative elementary volume (rev) within heterogeneous materials: A survey of scalar and vector metrics using porous

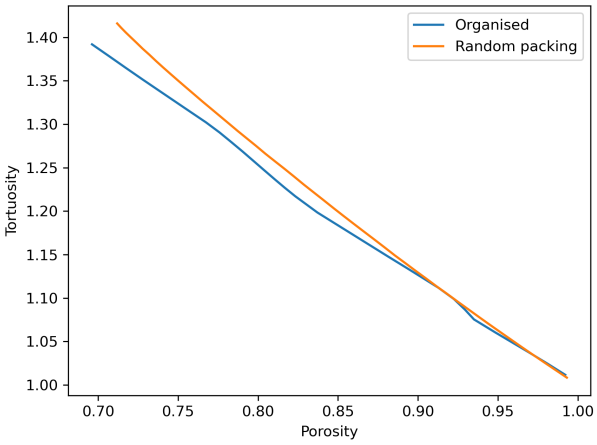

Figure A.14: The comparison of the tortuosity of the organised and random packing in relation to the porosity.

media as an example. Advances in Water Resources 192, 104762. doi:10.1016/j.advwatres.2024.104762.

Zwarts, S., Lesueur, M., 2024a. Homogenisation method based on energy conservation and independent of boundary conditions. Advances in Water Resources 183, 104603. URL: https://linkinghub.elsevier.com/retrieve/pii/S0309170823002385, doi:10.1016/j.advwatres.2023.104603.

Zwarts, S., Lesueur, M., 2024b. Predicting the Representative Elementary Volume by determining the evolution law of the convergence cone. Geomechanics for Energy and the Environment 40, 100594. URL: https://linkinghub.elsevier.com/retrieve/pii/S2352380824000613, doi:10.1016/j.gete.2024.100594.

Zwarts, S., Lindqwister, W., Lesueur, M., 2025. Rockmicro_minkowskis: A database of generated rock microstructures with minkowski functionals. https://github.com/sfzwarts/RockMicro_Minkowskis. Accessed: 2025-09-15.

Appendix A. Organised grid and Random Packings

For both the organised and random packings of circles, the tortuosity was evaluated across a range of packing fractions, as shown in Fig. A.14. The results reveal nearly identical trends for the two microstructural configurations, with minor differences in absolute values. This agreement indicates that the assumption of equivalence between organised and random packings is valid for estimating tortuosity in the granular packings. The small deviations are likely linked to the REV convergence of the organised grid, as reflected in the slight fluctuations observed in the data.

Appendix B. Effective microstructures

In order to assess the impact of using effective permeability estimates, we compute the permeability of samples based on the effective MFs. To obtain these, the inaccessible pore space within the sample—i.e., voids that do not percolate to the boundary—is filled, thereby creating an effective medium. This operation was carried out using the

596 regionprops and pore-filling utilities available in PoreSpy, which identify and remove isolated or invalid pores. An example of such microstructure is shown in Fig. B.16 The

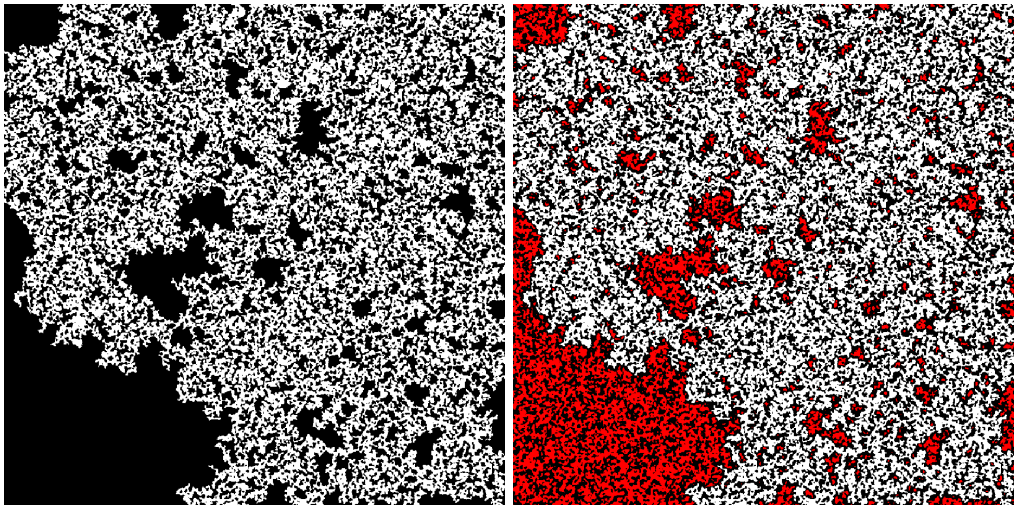

Figure B.15: An example of a cemented microstructure is shown, where inaccessible pore space has been filled with rock matrix. In these images, white corresponds to the solid phase and black to the pore space. The comparison on the right highlights the differences between the original and the filled microstructure, with the filled pores indicated in red.

597

598 MFs of this effective medium are then measured following the procedure described in
599 Sec.2. The resulting permeability estimates are presented in Fig.B.16.

600 We observe that the use of the effective medium mainly affects samples at lower
601 porosities, where the removal of non-percolating pores leads to different MF values.
602 However, the resulting permeability predictions based on these effective MFs do not
603 show an improvement in accuracy compared to the direct MF-based estimates.

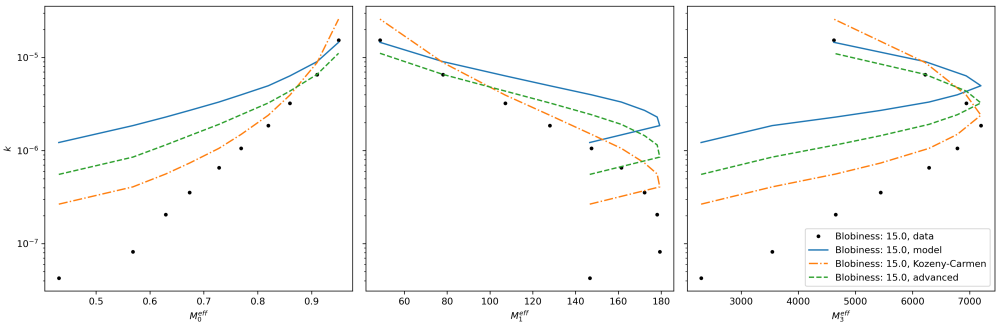

Figure B.16: The permeability of the effective cemented microstructure. The simulated data is shown with black markers, the model based on MFs is shown in a continuous blue line, the Kozeny-Carman prediction is shown with a dash-dot line in orange and the improved model with the green dashed line.